Exp. Theo. NANOTECHNOLOGY 10 (2026) 239-256 https://doi.org/10.56053/10.S.239

Effect of sintering temperature on electrical and structural properties for spinel ferrites prepared by sol-gel method

Atheer. I. Abd Ali[1], *Mohammed RASHEED*[2,*]

[1]Applied Sciences Department, University of Technology- Iraq, Baghdad, Iraq
[2]Production Engineering & Metallurgy College, University of Technology- Iraq, Baghdad, Iraq
[*]) Email: rasheed.mohammed40@yahoo.com

Received 17/11/2025, *Received in revised form* 15/12/2025, *Accepted* 28/12/2025, *Published* 15/2/2026

The structural and electrical properties of the nanoparticle spinel Ferrites with the general formula $Mn_xZn_{1-x}Fe_2O_4$ that are composed with a sol gel auto combustion have been analyzed by vector network analyzer (VNA), X-ray diffraction (XRD), and scanning electronic microscope (SEM). $MnZnFe_2O_4$ spinel Ferrites are prepared using high-purity manganese nitrate, iron nitrate, zinc nitrate, and citric acid. After being pressed at 100 M Pa by piston oil, the ferrite powder is sintered at three different sintering temperatures 900, 1000, and 1100 °C to create solid samples. The XRD pattern and SEM analysis showed that the samples are cubic spinel with an inhomogeneous grain size distribution. Several electrical parameters, such as DC resistivity, Impedance, dielectric constant with real and imaginary parts, and reactance depending on the scattering parameters, are calculated for the Mn-Zn ferrite in order to study its electrical properties. These calculations are done in the entire X-band range 8–12 GHz using a VAN.

Keywords: Mn–Zn ferrite; Sol-gel method; Ferromagnetic; Electrical; Structural.

1. INTRODUCTION

With the rapid development of modern technology, ferrites with spinel structures have gained significant importance due to their high capability to absorb electromagnetic waves and their versatile chemical composition of the form AB_2O_4, where A and B represent different metal cations. These ferrites are typically composed of iron oxides such as hematite (Fe_2O_3) and magnetite (Fe_3O_4), combined with other metal oxides including CuO, NiO, MnO, CoO, and ZnO [1–4]. Various synthesis techniques have been employed for the preparation of spinel ferrites, such as conventional ceramic methods, hydrothermal processes, pulsed laser deposition, and sol–gel techniques. Among these, the

sol–gel method is particularly attractive due to its advantages of low processing temperature, high chemical homogeneity, and better control over particle size and composition [5,6]. Consequently, spinel ferrites have become essential materials for numerous electronic applications, including capacitors, transmitters and receivers, soft magnetic devices, and electromagnetic interference suppression filters [7–10]. High-frequency and microwave functional properties of spinnel ferrites are mostly controlled by their microstructure parameters such as grain size, porosity, and cations distribution which in turn are highly sensitive to the processing conditions especially sintering temperature [11–13]. Excessive sintering could lead to the overgrowth of grain boundaries or porosity and consequently result in better carrier conduction hopping but bad dielectric and impedance properties. Even though ferrites are generally considered to be insulating ferrimagnetic ceramic materials [17, 18], their electrical response at microwave can be somewhat different depending on synthesis and thermal treatment of the material [19, 20]. For the high frequency electrical characterization, VNA (vector network analyzer) measurement provides valuable information with scattering parameters such as reflection, transmission resistance and impedance coefficients [21–23]. In this regime, electrical response of ferrite under X-band frequency (8–12 GHz) is investigated though S_{21} and S_{22} parameters. Although a number of works dedicated to Mn–Zn ferrites prepared by chemical routes is reported, most of them just pay attention to the study of magnetic and low frequency electrical properties. It is very rare to get complete studies systematically correlating the sintering temperature with microwave-frequency electrical properties: the related impedance, real and imaginary part of dielectric constant and reactance obtained from the scattering parameters. Furthermore, correlation of these electrical properties with structural transformation as followed through X-ray diffraction (XRD) and scanning electron microscopy (SEM) for the case of sol–gel auto-combusted Mn–Zn ferrites is not extensively addressed. This lack of collective knowledge prevents to optimize Mn–Zn ferrites for emerging microwave and communication devices 24, 25]. Therefore, in the present work we study the effect of sintering temperature on structural and electrical properties of MnZn spinel ferrite nanoparticles (MNPs) prepared by sol–gel auto-combustion technique. Sintered ferrite powders are synthesized at 900, 1000 and 1100 °C to study the influence of calcination temperature on phase formation, crystallinity and grain morphology using XRD and SEM. Furthermore, the key electrical characteristics including DC resistivity, impedance, dielectric constant (both real and imaginary parts), reactance are evaluated in 8 12 GHz range based on a vector network analyzer. This work will also be beneficial to the comprehension of the relationship between microstructure and high-frequency electrical properties, and optimising Mn–Zn ferrites in microwave devices and electromagnetic absorbing materials.

2. EXPERIMENTAL DETAILS

2.1 The sample preparation

To produce $Mn_{0.5}Zn_{0.5}Fe_2O_4$, the raw materials with very high purity are chosen so as to refrain any effect on the compound properties. Table 1 illustrates the raw materials which are utilized in the present work. After determining the atomic weights, these raw materials are mixed with double-distilled water (80 ml) in a glass beaker that is heat-resistant. The mixture is then homogenized by constant stirring on a hot plate using magnetic stirrers. The pH solution is adjusted to (~7) by adding ammonia solution, and it is then heated for 30 minutes at 50°C on a hot plate. The temperature is increased to (90ºC) within continuous heating for more than (2 hrs.). The sol is first transformed into gel and then dried at 120°C. To create a structure of fluffy loose, the dried gel is burned in a self-propagating combustion manner until all of the gel had been consumed. In order to achieve a better crystallization with homogeneous cation distribution through the spinel crystallite, the burnt-ash is calcined at (500°C) for (3 hours). In order to obtain the samples as a parallelogram measuring (2.41.21.2) cm, the powder is pressed at (102 MPa) by the piston oil. The samples are heated to three different sintering temperatures (900°C, 1000°C, and 1100°C) for six hours at a heating rate of

50°C/min, after which they are removed from the furnace to cool gradually. Finally, the samples are refined to get the dimensions (2.2×31.0×1.0 cm).

Table 1 The raw materials.

Raw materials	The purity
$Cu(NO_3)_2.6H_2O$	99 %
$Mn(NO_3)_2$	98%
$Zn(NO_3)_2.6H_2O$	98%
$Fe(NO_3)_3.9H_2O$	97%

2.2 Sample characterizations

2.2.1 X-RAY diffraction measurement

The structural analysis is employed for the prepared samples after sintering, to investigate the crystal structure by x-ray diffraction pattern (XRD) utilizing the radiation of Cu-Kα with wavelength λ = 1.54060 Å. The samples are measured using an XRD-6000 device, which is made in Japan by SHIMADZU, with a Braggs angle range of approximately (2θ=10–80). Eq. 1, which represents Bragg's law [26-28], can be used to calculate the distance between the atomic levels (d) of the prepared models. The Standard Specifications Table (ASTM) is also approved in the comparison process to determine the levels associated with growth of spinel structure Ferrites [29-31].

$$n\lambda = d \sin(\theta) \quad (1)$$

$$a = d\sqrt{h^2 + k^2 + l^2} \quad (2)$$

The lattice parameter (a) can be determined using equation (3-5), which represents the cubic system standard relation [32-34], where (n) refers to integer, (λ) represents the wavelength, (θ) is the X-ray incidence angle and (d) is the distance between the levels of crystal. The inter planer distance (d) is determined, and then the resultant x-ray patterns are compared with international standard (ICDD), which is the American Standard for Testing Materials (ASTM) [35]. Normally, XRD is applied to compute various parameters that could be employed to clarify the studies of the prepared samples.

a) Average Crystal Size (C.S.): Scherer's formula has been used to estimate the average Crystal size (C.S.), it is one of the many line profile analysis techniques represented by the single line technique, which is based on a Voigt function to calculate the size-strain parameters (crystallite sizes and micro strains) [36-40].

$$C.S. = \frac{0.94\lambda}{\Delta \cos(\theta)} \quad (3)$$

Where Δ represents the full width half maximum (FWHM), λ refers to the XRD wavelength and θ is the diffraction angle of XRD peak.

b) Micro Strains (MS): The micro strains, which are measured in parts per million, are brought about by the sintering of the samples. Additionally, the stretching or compression of the lattice strain, which may be brought about by modifications to the atoms' displacements relative to the reference lattice, would be investigated [13, 41-45]. The micro strain could be computed using the formula [9, 46-50]

$$MS = \left|\frac{a_{ASTM} - a_{XRD}}{a_{ASTM}}\right| \times 100\% \quad (4)$$

c) FWHM: is the line width at the half height for the intensity peak and is usually measured in (degree)unit.

d) By using the equation (6), the density is computed from the XRD pattern parameters, along with the porosity (P) that is calculated using bulk density (ρ_{bulk}) of the prepared samples as illustrated in Eq. 7 [11, 51-53]

$$\rho_{bulk} = \frac{m}{v} \quad (5)$$

$$\rho_{theo} = \frac{8.M}{N_A.a^3} \quad (6)$$

$$P(\%) = \left(1 - \frac{\rho_{bulk}}{\rho_{theo}}\right) \quad (7)$$

where (ρ_{theo}) refers to the theoretical density, (M) refers to the molecular mass, (N_A) represents the Avogadro's number and (a) is the constant of lattice. The number 8 in equation (6) refers to the number of molecules in the unit cell.

2.2.2 Measurement of electrical properties

The measurement of electrical properties is personalized by using vector network analyzer devise (VNA) type of Anritsu MS4642A-20GHz, in the reign of all X-band frequencies (8-12 GHz).
The DC electrical conductivity (σ_{DC}) is determined by using the following equation [19, 54].

$$\sigma_{DC} = \frac{d}{RA} \quad (8)$$

where (d) is thickness of the sample pellet in (m), (R) is the sample resistance in unit (Ω), (A) refers to the sample pellet area in (m^2).
Drift mobility (μ) is computed by utilizing the following relation [19, 55]

$$\mu = \frac{\sigma_{Dc}}{ne} \quad (9)$$

where (e) is the electron charge, (n) is the concentration of charge carrier that could be calculated from Eq. 10 [19, 55]

$$n = \frac{N_A \rho_{bulk} N_{Fe}}{M} \quad (10)$$

Eq. 11, which used to calculate the real part of the dielectric constant ((ε'), allowed Eq. 12 to be used to calculate the imaginary part of the dielectric constant (ε'') [18, 55]

$$\varepsilon' = \frac{Cd}{\varepsilon_\circ A} \quad (11)$$

where (C) represents the capacitance [51]

$$\varepsilon'' = \varepsilon' \tan\delta \quad (12)$$

where (tanδ) is the dielectric loss tangent that is calculated using Eq. 13 [20, 40]

$$\tan\delta = \cot(\phi) \quad (13)$$

where (ϕ) is the phase angle in degree.
The Impedance real part (Z') and imaginary part (Z'') could be determined using the equations below (14-15) [49]

$$Z' = |Z|\cos(\phi) \quad (14)$$

$$Z'' = |Z|\sin(\phi) \quad (15)$$

where (Z) is the Impedance.
From dielectric constant, the AC conductivity is calculated when employing the equation (16) [12]

$$\sigma_{Ac} = 2\pi f \varepsilon' \varepsilon_\circ \tan\delta \quad (16)$$

where (σ_{AC}) represents the AC conductivity, (f) denots to the frequency in (HZ), ($\varepsilon_\circ$) is the free space permittivity, this leads to evaluate the electrical modulus (M′ and M″), real and imaginary parts of respectively using the equation (17-18) [13-17]

$$M' = \frac{\varepsilon'}{\varepsilon''^2 + \varepsilon''^2} \quad (17)$$

$$M'' = \frac{\varepsilon''}{\varepsilon'^2 + \varepsilon''^2} \quad (18)$$

The quality factor (Q) introduced as the reciprocal of loss factor as in Eq. 19 [8]

$$Q = \frac{1}{\tan(\delta)} \quad (19)$$

2.2.3 Antibacterial activity

The antibacterial activity of $MnxZn_{1-x}Fe_2O_4$ nanoparticles (NPs) is evaluated against Gram-negative *Escherichia coli* (*E. coli*) and Gram-positive *Staphylococcus aureus* (*S. aureus*) using the agar diffusion method (ADM). Sterile Mueller–Hinton agar plates are uniformly inoculated with bacterial suspensions adjusted to a 0.5 McFarland standard (approximately 1.5×10^8 CFU/mL). Wells with a

diameter of 6 mm are aseptically punched into the agar and filled with a fixed volume of the $MnxZn_{1-x}Fe_2O_4$ nanoparticle suspension. The plates are incubated at 37 °C for 24 h, after which the antibacterial efficacy is determined by measuring the diameter of the inhibition zones (in millimeters) formed around each well. For this assessment, circular samples of $MnxZn_{1-x}Fe_2O_4$ nanoparticles sintered at 1100 °C are employed.

2.2.4 Surface morphology

The images of scanning electron microscopy (SEM) for ferrite samples are used to investigate the distribution pattern of the particle or grain size, crystal morphology and surface nature. Scanning electron microscopy measurements show that all prepared samples consist of inhomogeneous grain size distribution, which vary from (10 nm to 500 nm), as shown in Figure 1.

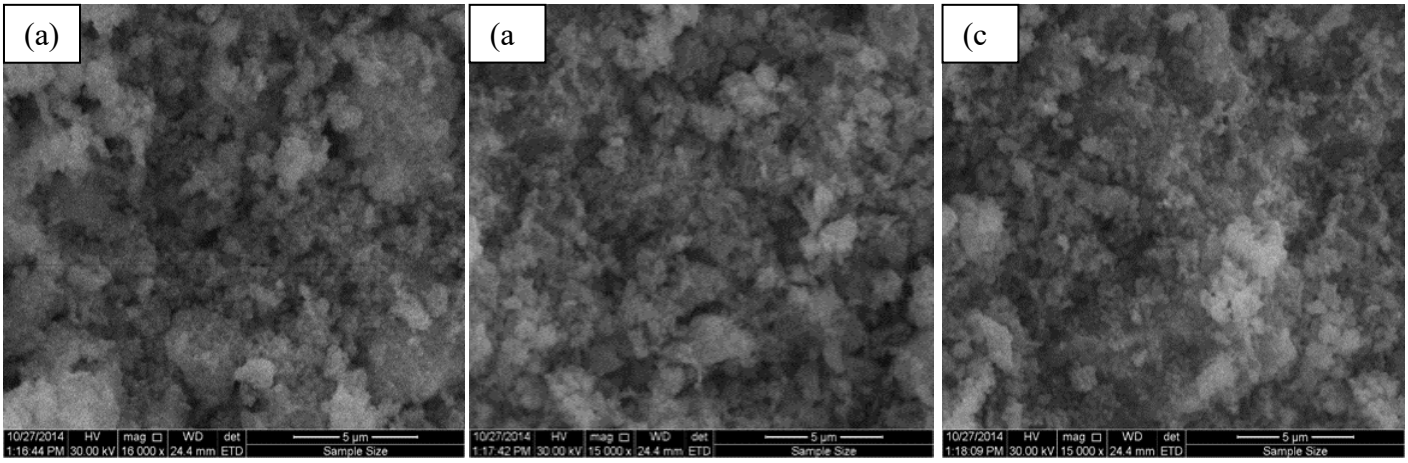

Figure 1 SEM micrographs of $Mn_{0.5}Zn_{0.5}Fe_2O_4$ sample; prepared at (a) 900 ºC, (b) at 1000 ºC, and (c) 1100 ºC using sol-gel methods.

3. RESULTS AND DISCUSSIONS

The results of the X-ray diffraction measurements showed that all prepared samples have a polycrystalline structure and match perfectly with (ASTM) (ICDD cards 01-071-4919 AND 04-001-9287), as shown in and Fig. 2 and Table 2, which are related to the formation of the cubic spinel structure. The values of Millar indices (h k l), which diffracted from X-ray, are (220), (400),(440), (511), and the preferred plan is (311). The X-ray diffraction pattern results illustrate that the increasing in sintering temperature led to a decrease in the Average Crystal Size and porosity, which in turn led to an increase in the bulk density. It is natural that the temperature increasing will lead to an increase in the Micro Strains.

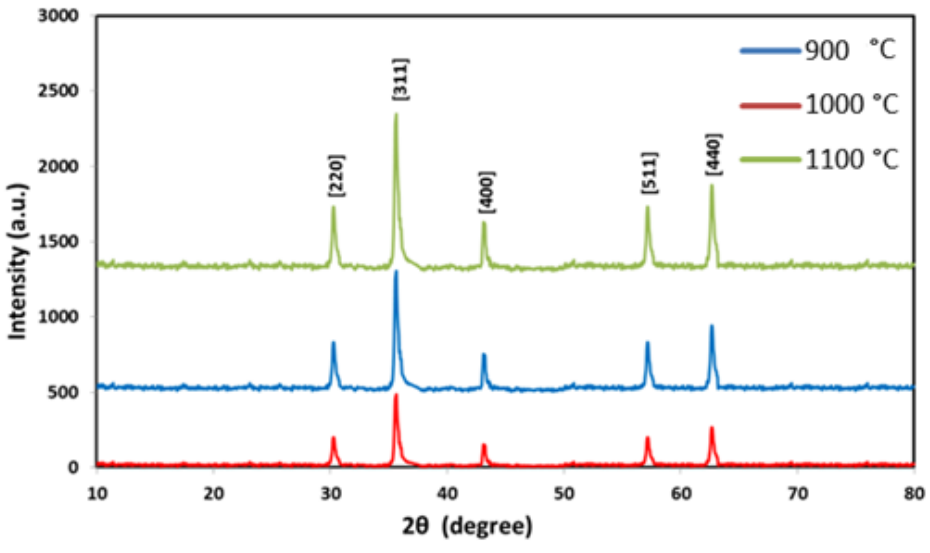

Figure 2 X-ray pattern of $Mn_{0.5}Zn_{0.5}Fe_2O_4$ samples investigate by sol-gel technique at various sintering temperature.

Table 2 XRD parameters for as-prepared samples.

Samples	(hkl)	$2\theta^0_{XRD}$	β (°)	D_{ave} (nm)
	(220)	32.2	0.546	14.595
	(311)	35.55	0.546	14.465
S1-900 °C	(400)	43.1	0.462	16.698
	(511)	57.1	0.546	13.343
	(440)	62.2	0.546	13.007
	(220)	32.2	0.571	13.951
	(311)	35.55	0.571	13.827
S2-1000 °C	(400)	43.1	0.487	15.834
	(511)	57.1	0.571	12.755
	(440)	62.2	0.571	12.433
	(220)	32.2	0.588	13.552
	(311)	35.55	0.588	13.432
S3-1100 °C	(400)	43.1	0.504	15.306
	(511)	57.1	0.588	12.390
	(440)	62.2	0.588	12.078

Figures 3-6 show aforementioned results. Although the results of the electrical measurements indicated a direct relationship between the DC conductivity and the frequency, the effect of increasing the sintering temperature resulted in an increase in the DC conductivity, and since DC resistivity is the reciprocal of the DC conductivity, the relationship of the frequency with each of the DC resistivity, reactance, and impedance is an inverse relationship with the frequency, and the increasing in the sintering temperature led to their decrease, the Figures 7-10 show this analysis.

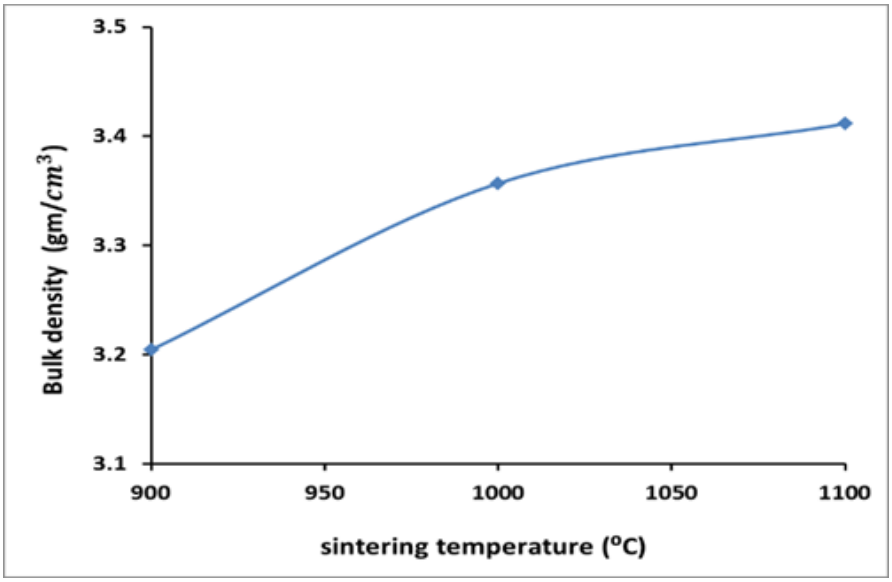

Figure 3 Sintering temperature effect with bulk density.

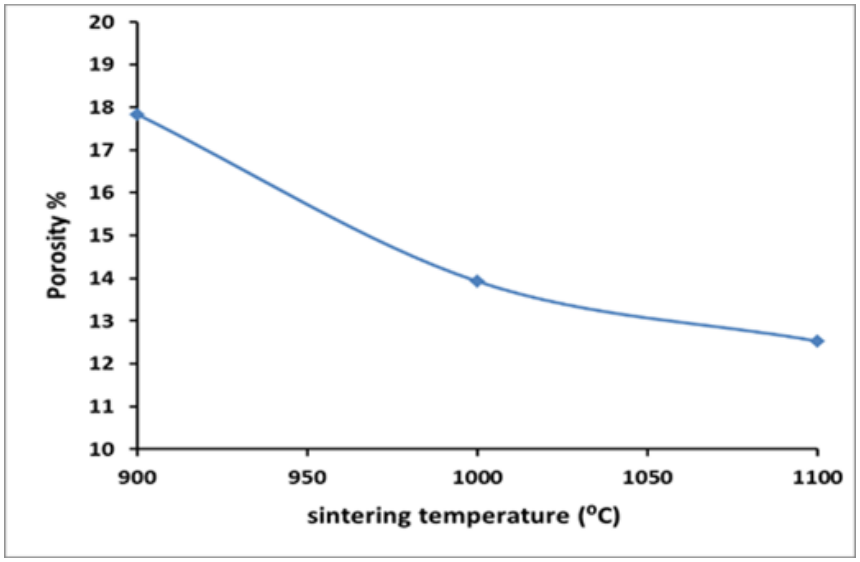

Figure 4 Relationship between sintering temperature with porosity.

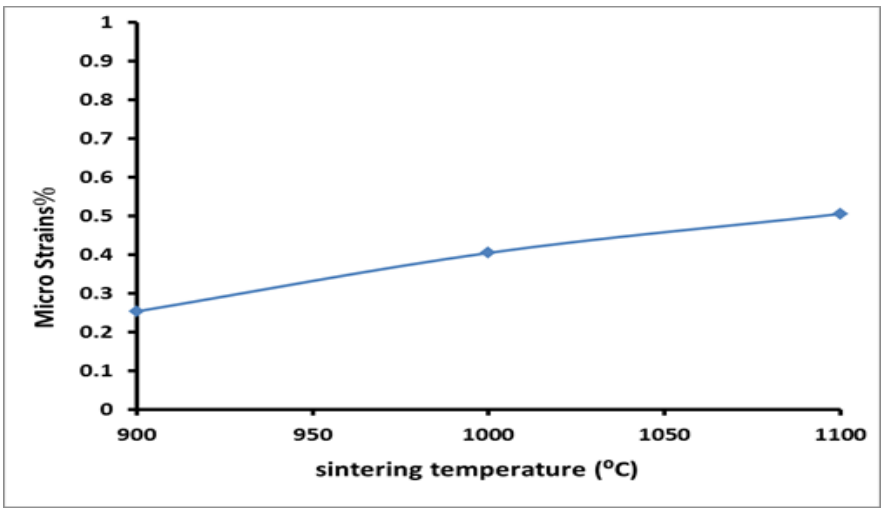

Figure 5 Effect of sintering temperature with nano strains.

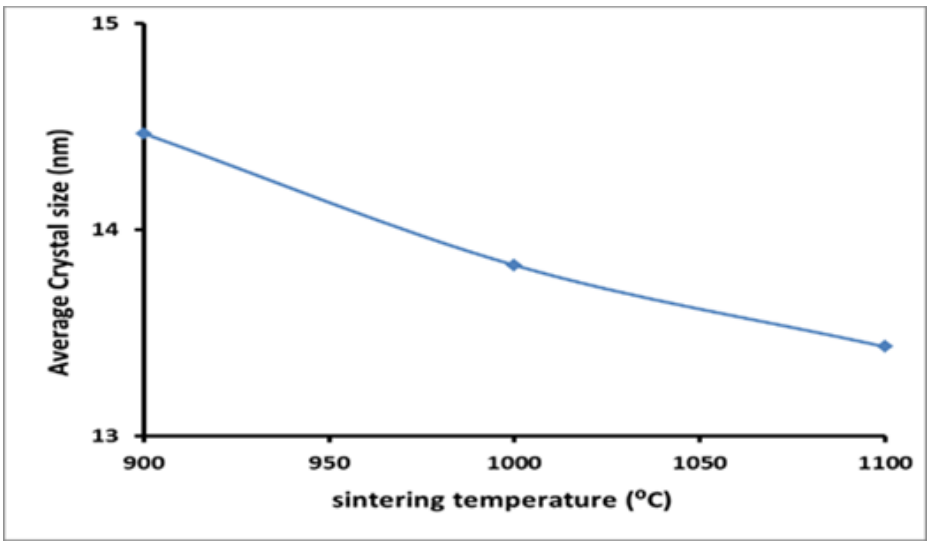

Figure 6 Effect of sintering temperature with the average crystal size.

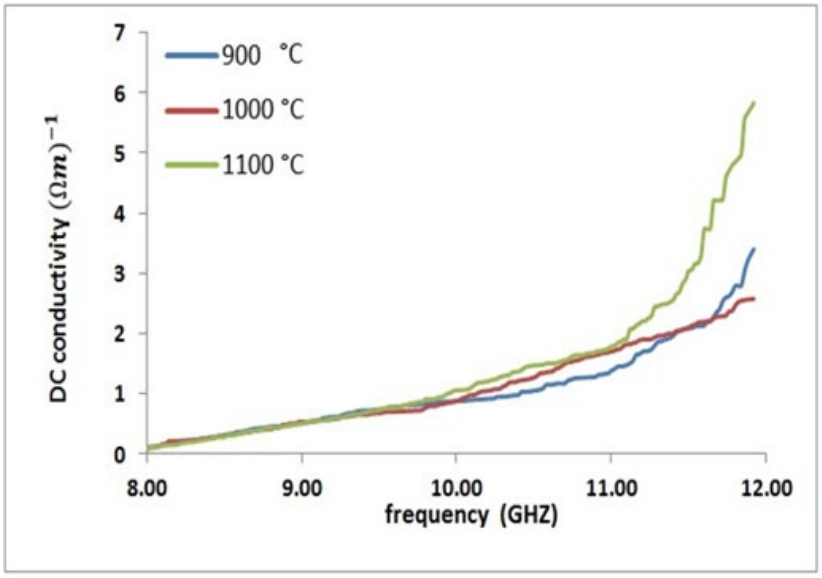

Figure 7 DC conductivity of $Mn_{0.5}Zn_{0.5}Fe_2O_4$ samples with different sintering temperature.

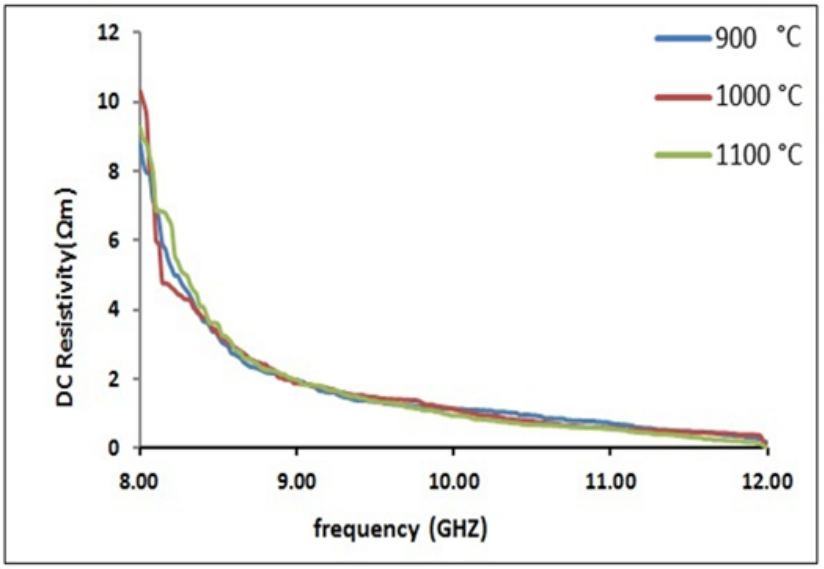

Figure 8 DC Resistivity of $Mn_{0.5}Zn_{0.5}Fe_2O_4$ samples with different sintering temperature.

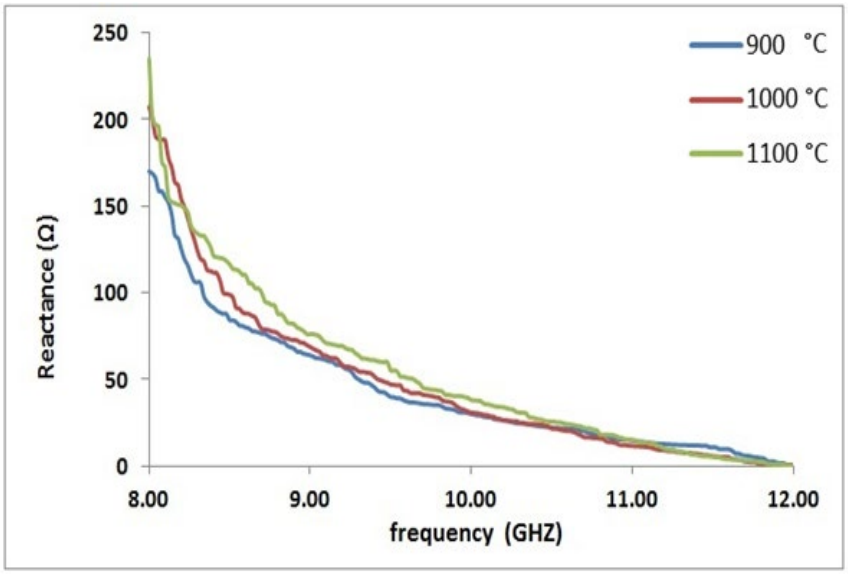

Figure 9 Reactance of $Mn_{0.5}Zn_{0.5}Fe_2O_4$ samples with different sintering temperature.

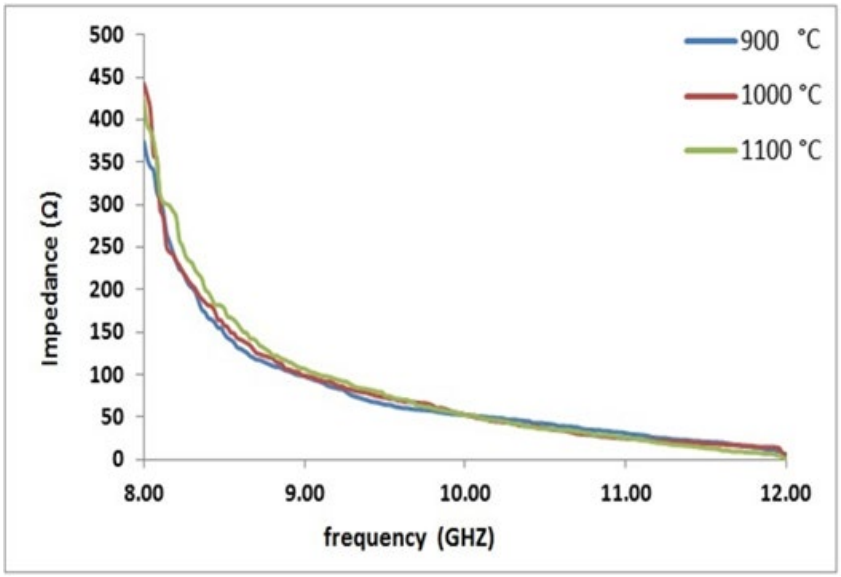

Figure 10 Impedance of $Mn_{0.5}Zn_{0.5}Fe_2O_4$ samples with different sintering temperature.

Due to the fact that the impedance is a function of both the real (Z') and imaginary (Z") parts, Figures 11 and 12 show that the behaviour of the curve for each of these parts is decreasing with increasing frequency, and the effect of increasing the sintering temperature is different. The real part thus demonstrated that lowering the sintering temperature reduces the values of the real part of the impedance for frequencies below (11MHz) and for frequencies greater than (11MHz). While there is no significant effect on the sintering temperature increasing for the imaginary part of the impedance, this behaviour is reversed.

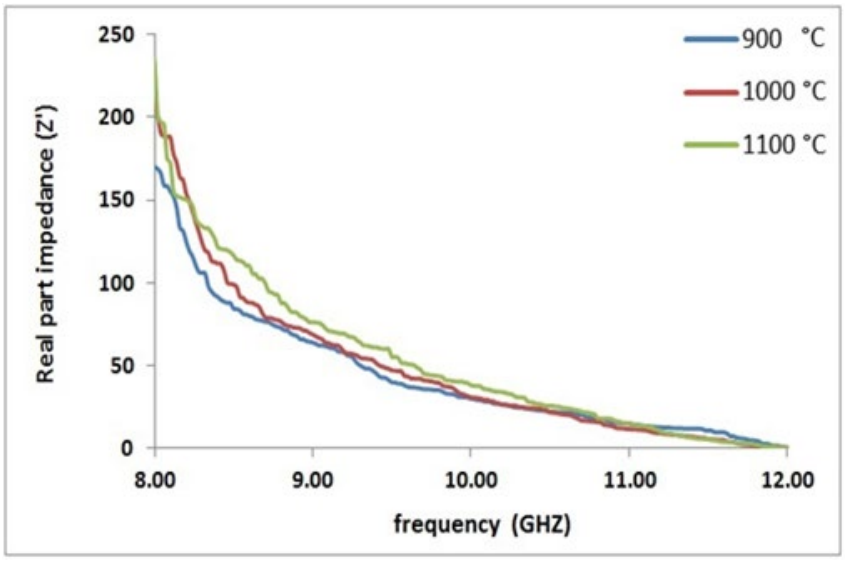

Figure 11 Real part impedance (Z') of $Mn_{0.5}Zn_{0.5}Fe_2O_4$ samples with different sintering temperature.

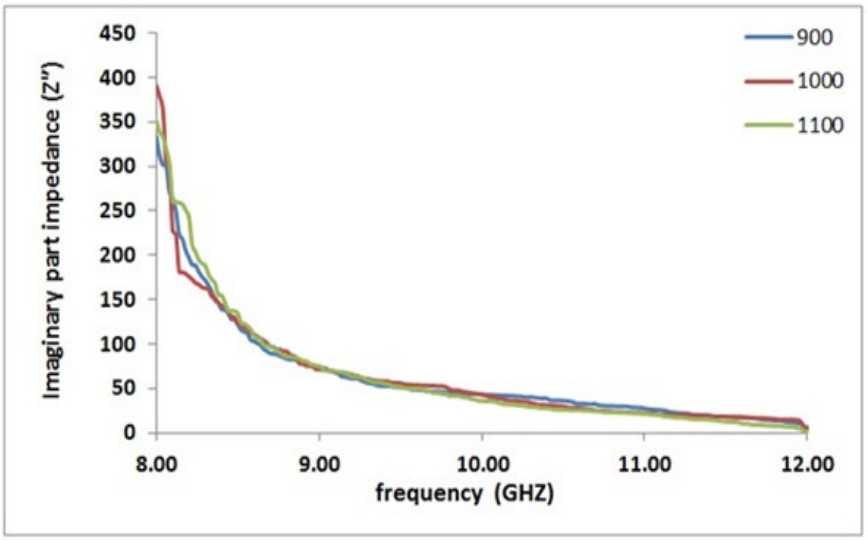

Figure 12 Imaginary part impedance (Z'') of $Mn_{0.5}Zn_{0.5}Fe_2O_4$ samples with different sintering temperature.

Figure 13 shows the behavior of the Gaussian distribution of the real part of dielectric modulus (M′), as it had a local maximum at the frequency (10.5) at the sintering temperature (1000 ^oC and 1100 ^oC), while the temperature (900 ^oC) is the local maximum at the frequency (11.5 MHz).

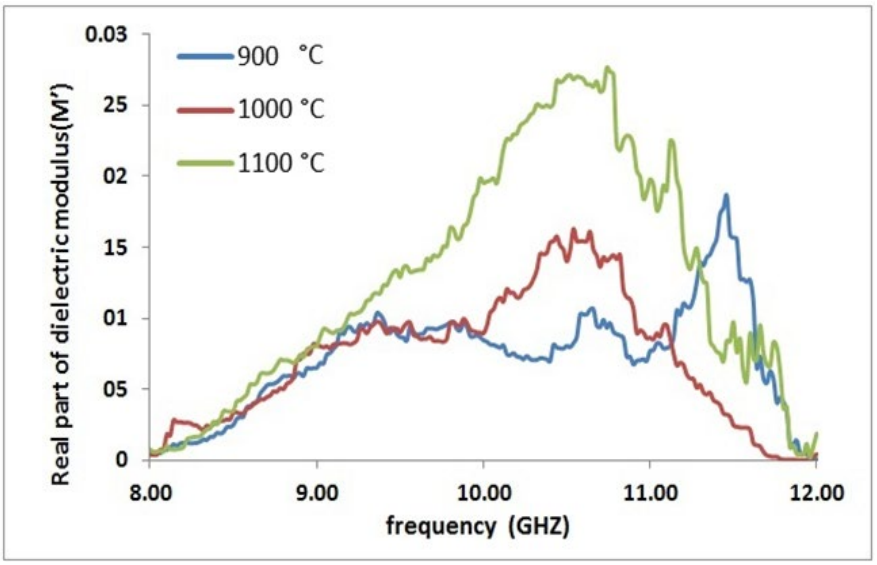

Figure 13 Real part of dielectric modulus(M′) for $Mn_{0.5}Zn_{0.5}Fe_2O_4$ samples with frequency.

Regarding the imaginary part of dielectric modulus (M″) depicted in Figure (13), it demonstrated an erratically increasing trend for frequencies greater than (12MHz) for the sintering temperature (1100), and the Gaussian distribution's behavior is not balanced as it is for the real part of dielectric modulus (M').

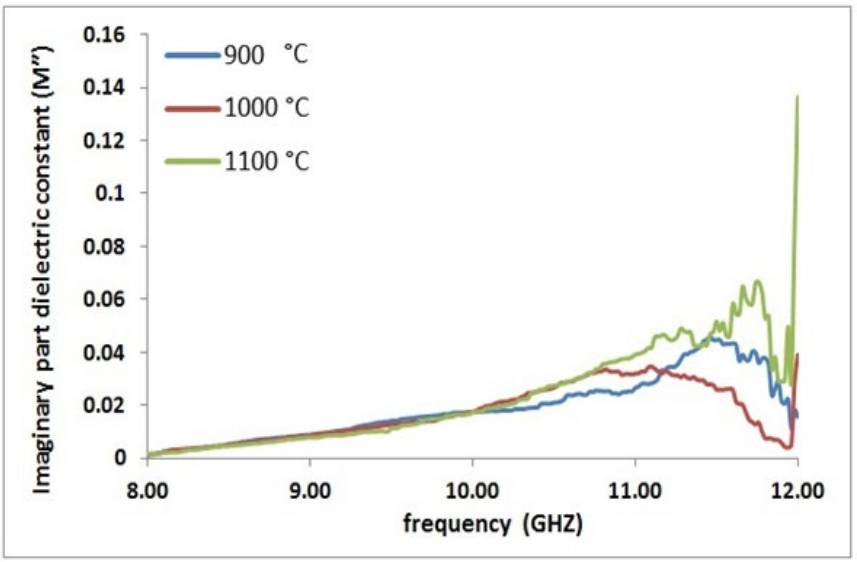

Figure 14 Frequency versus imaginary part dielectric modulus (M″) for $Mn_{0.5}Zn_{0.5}Fe_2O_4$ samples.

Figure 15 shows that as the sintering temperature increased, the number of charge carriers increased as well. This result is consistent with the DC conductivity in Figure 6.

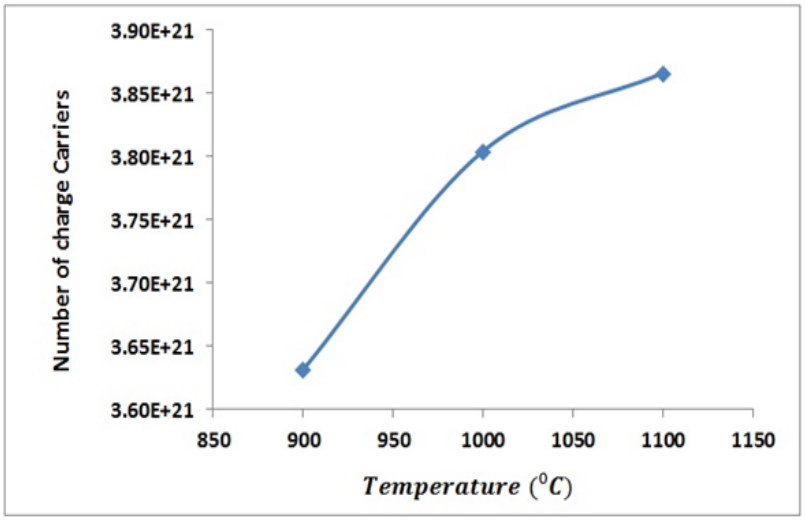

Figure 15 Charge carriers' number of $Mn_{0.5}Zn_{0.5}Fe_2O_4$ samples with different sintering temperature.

Figure 16 demonstrates that as Drift mobility increased, frequency and sintering temperature also increased.

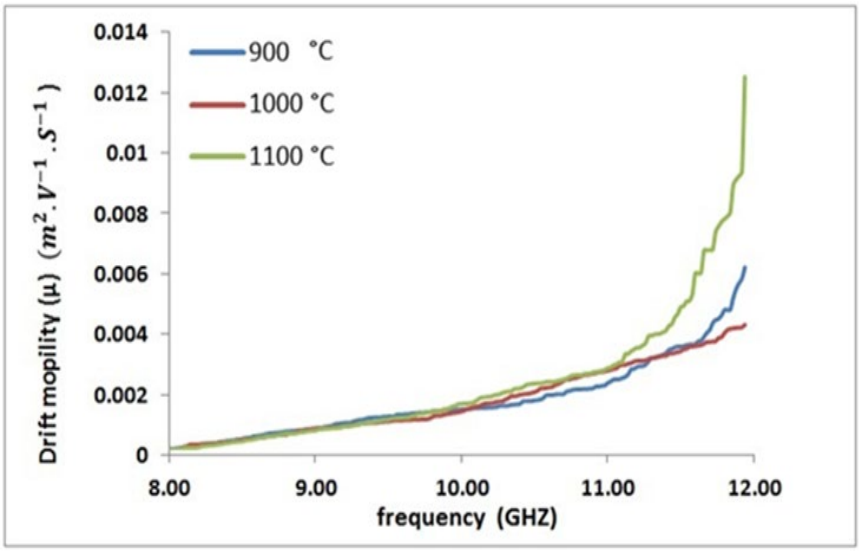

Figure 16 Drift mobility (μ) of $Mn_{0.5}Zn_{0.5}Fe_2O_4$ samples as a function to sintering temperature

Figure 17 shows the effect of the quality factor's Gaussian distribution, with the maximum values occurring in the frequency ranges of 8 to 9 GHz. Figure 18 shows an increase in dielectric loss (tan (δ)), particularly for frequencies greater than (11.75).

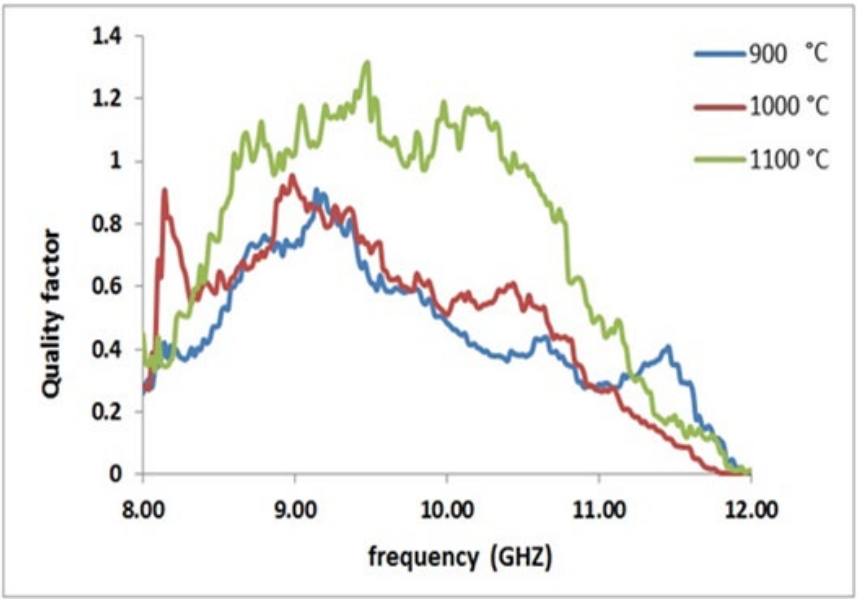

Figure 17 Quality factor of $Mn_{0.5}Zn_{0.5}Fe_2O_4$ samples with sintering temperature.

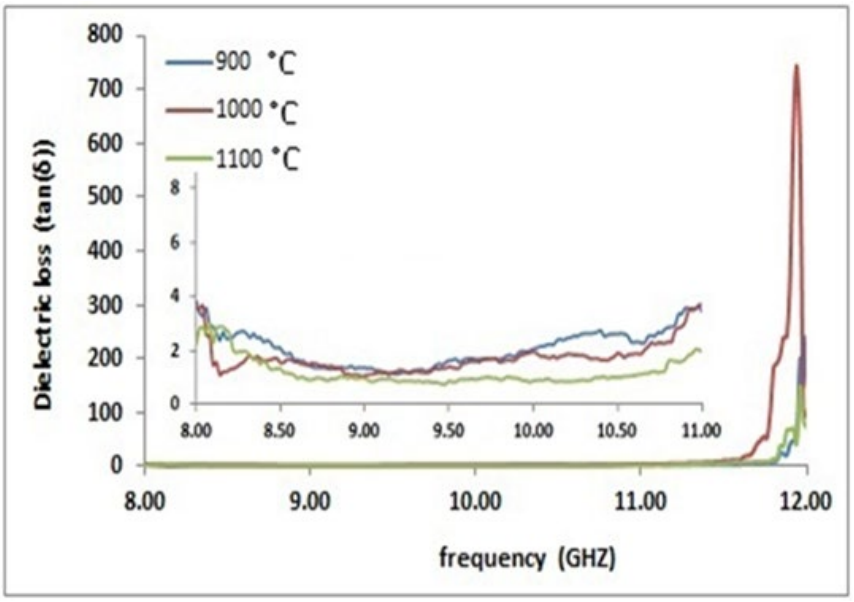

Figure 18 Relation between Dielectric losses with sintering temperature for $Mn_{0.5}Zn_{0.5}Fe_2O_4$ samples

5. ANTIBACTERIAL ACTIVITY

The agar diffusion results demonstrate that the $MnxZn_{1-x}Fe_2O_4$ nanoparticles sintered at 1100 °C exhibit clear antibacterial activity against both Gram-negative *Escherichia coli* and Gram-positive *Staphylococcus aureus*. The formation of distinct inhibition zones around the wells confirms the effective diffusion of active species from the nanoparticle suspension into the agar medium and their interaction with bacterial cells. The measured zone of inhibition (ZOI) of 10.70 mm for *E. coli* indicates a slightly stronger antibacterial response compared to *S. aureus*. The enhanced susceptibility of *E. coli* relative to *S. aureus* can be attributed to differences in cell wall structure. Gram-negative bacteria possess a thinner peptidoglycan layer, which may facilitate greater interaction between the

bacterial membrane and the ferrite nanoparticles or the reactive oxygen species (ROS) generated at the nanoparticle surface. In contrast, the thicker peptidoglycan layer in Gram-positive *S. aureus* acts as a partial barrier, resulting in a marginally reduced ZOI of 9.95 mm. Furthermore, the observed antibacterial performance may be associated with the nanoscale particle size, improved crystallinity, and surface defects induced by high-temperature sintering, which can enhance ROS generation and metal ion release. These mechanisms collectively contribute to membrane disruption, protein denaturation, and inhibition of bacterial metabolic activity. Overall, the ADM results confirm that $MnxZn_{1-x}Fe_2O_4$ nanoparticles synthesized via the sol–gel method and sintered at 1100 °C possess promising antibacterial properties, making them suitable candidates for biomedical and antimicrobial applications.

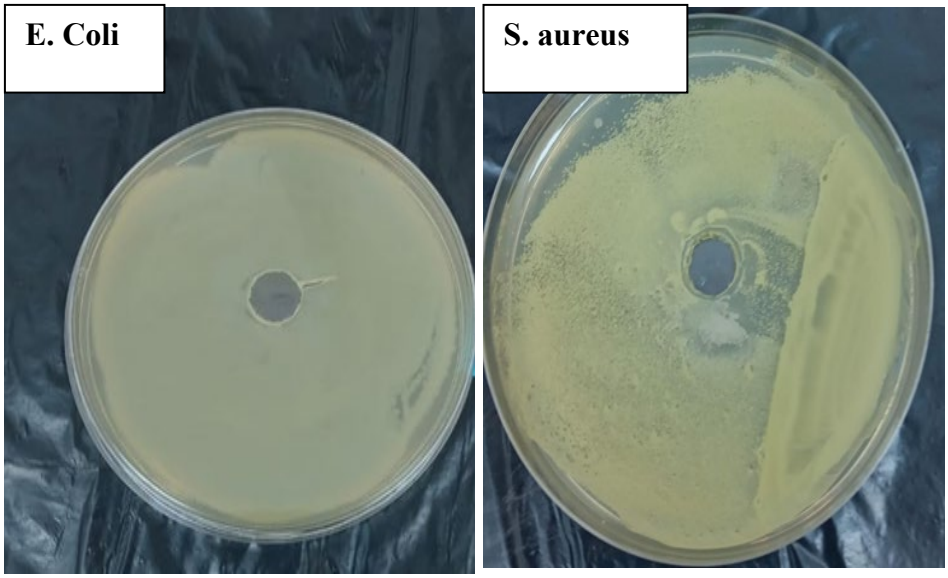

Figure 19 Agar diffusion method (ADM) showing the antibacterial activity of $MnxZn_{1-x}Fe_2O_4$ nanoparticles sintered at 1100 °C against (a) *Escherichia coli* with a zone of inhibition (ZOI) of 10.70 mm and (b) *Staphylococcus aureus* with a ZOI of 9.95 mm

6. CONCLUSIONS

In this manuscript, the effect of changing the sintering temperature on the electrical and structural properties of $Mn_{0.5}Zn_{0.5}Fe_2O_4$ ferrite prepared by sol-gel method was studied while maintaining control over the pH and temperature of the solutions during the preparation process. The final results were detrimental to our noticeable improvement in the structural properties, which led to a clear improvement in the electrical properties when the sintering temperature is raised. It was observed that the number of charge carriers increased with the increase in the sintering temperature, the increase in the sintering temperature also led to a decrease in the average crystal size, and thus led to decrease both porosity and Micro Strains.

References

[1] J. Iqbal, M. Ahmad, Z. T. Meydan, Y. Melikhov. J. appl. Phy. 111 (2012) 033906 https://doi.org/10.1063/1.3676438
[2] M. Ismail, N. Jaber. Iraq. J. Phys. 16 (2018) 140 https://doi.org/10.216233/ijp.v16i36.31
[3] C. Venkataraju, G. Sathishkumar, K. Sivakumar, J. Magnet. Mat. 322 (2010) 230 https://doi.org/10.4236/msa.2010.11004

[4] L. Zhao et al. J. Magn. Magn. Mater. 301 (2006) 445 https://doi.org/10.1122/j.jmmm.2006.07.013
[5] S. H. Lafta. Mater. Res. Express 6 (2019) 046103 https://doi.org/10.1088/2053-1591/aafb80
[6] T. Nakamura, Y. Okano. J. Appl. Phys. 79 (1996) 7129 https://doi.org/10.1061/1.317480
[7] S. A. Mazen, S. F. Mansour, and H. M. Zaki, Cryst. Res. Technol. 38 (2003) 471 https://doi.org/10.1002/crat.200310059
[8] A. M. Nicolson. IEEE Transactions on Instrumentation and Measurement 17 (1968) 395 https://doi.org/10.1109/tim.1968.4313741
[9] C. Gümüs, O.M.Ozkendir, H. Kavak, and Y. Ufuktepe, J. Optoelectron. Adv. Mater. 8 (2006) 299 https://doi.org/10.4323/rjlm.2010.203
[10] E. K. Al-Shakarchi et sl. J. Supercond. Nov. Magn. 29 (2016) 923 https://doi.org/10.1007/s10948-015-3334-9
[11] J. Baker-Jarvis, E. J. Vanzura, and W. A. Kissick, IEEE Trans. Microw. Theory Techn. 38 (1990) 1096 https://doi.org/10.1109/22.57336.
[12] R. B. Schulz, V. C. Plantz, and D. R. Brush, IEEE Trans. Electromagn. Compat. 30 (1988) 187 https://doi.org/10.1109/15.3297
[13] A. P. Singh, M. Mishra, A. Chandra, and S. K. Dhawan. Nanotech. 22 (2011) 465701 https://doi.org/10.1088/0957-4484/22/46/465701
[14] Z. Yang et al. Polymers, 11(8) (2019) 1252. https://doi.org/10.3390/polym11081252
[15] J. H. Shim et al. Phy. Rev. B 73 (2006) 064404 https://doi.org/10.1103/PhysRevB.73.064404
[16] D. Mane et al. J. Sol-Gel Sci. Technol. 58 (2011) 70 https://doi.org/10.1007/s10971-010-2357-8
[17] M. A. Dar, M.K. Batoo, K.M., RK Kotnala. Journal of Alloys and Compounds 632 (2015) 307 20 https://doi.org/10.1016/j.jallcom.2015.01.190
[18] I. Alshalal, H. M. I. Al-Zuhairi, A. A. Abtan, M. Rasheed, M. K. Asmail. J. Mech. Behav. Mater. 32 (2023) 1 https://doi.org/10.1515/jmbm-2022-0280
[19] M. Sellam, M. Rasheed, S. Azizi, T. Saidani. Ceram. Int. 50 (2024) 20917 https://doi.org/10.1016/j.ceramint.2024.03.094
[20] O. Alabdali, S. Shihab, M. Rasheed, T. Rashid. 3rd inter. Scient. conf. alkafeel univ. (ISCKU 2021) (2022). https://doi.org/10.1063/5.0066860
[21] M. Rasheed, O. Alabdali, S. Shihab, A. Rashid, T. Rashid, J. Phys.: Conf. Ser. 1999 (2021) 012078 https://doi.org/10.1088/1742-6596/1999/1/012078
[22] N. Assoudi et al. Opt. Quant. Electron. 54 (2022) 9 https://doi.org/10.1007/s11082-022-03927-x
[23] R. Jalal, S. Shihab, M.A. Alhadi, M. Rasheed, J. Phys.: Conf. Ser. 1660 (2020) 012090 https://doi.org/10.1088/1742-6596/1660/1/012090
[24] S. Shihab, M. Rasheed, O. Alabdali, A.A. Abdulrahman, J. Phys.: Conf. Ser. 1879 (2021) 022120 https://doi.org/10.1088/1742-6596/1879/2/022120
[25] A. Keziz, M. Heraiz, M. RASHEED, A. Oueslati. Mater Chem. Phys. 325 (2024) 129757 https://doi.org/10.1016/j.matchemphys.2024.129757
[26] D. Kherifi, A. Keziz, M. Rasheed, A. Oueslati. Ceram. Int. 50 (2024) 30175 https://doi.org/10.1016/j.ceramint.2024.05.317
[27] A. Jaber, M. Ismael, T. Rashid, M. A. Sarhan, M. Rasheed, I. M. Sala. Eureka: Phys. Eng. 4 (2023) 29 https://doi.org/10.21303/2461-4262.2023.002770
[28] T. Rashid, M. M. Mokji, M. Rasheed. J. Optics 11 (2024) 39 https://doi.org/10.1007/s12596-024-02080-w
[29] H. K. Aity, E. Dhahri, M. Rasheed. Ceram. Int. 50 (2024) 54666 https://doi.org/10.1016/j.ceramint.2024.10.324
[30] M. Rasheed, S. Shihab, O. Alabdali, A. Rashid, T. Rashid, J. Phys.: Conf. Ser. 1999 (2021) 012077 https://doi.org/10.1088/1742-6596/1999/1/012077
[31] M. Rasheed, M. Nuhad Al-Darraji, S. Shihab, A. Rashid, T. Rashid. J. Phys.: Conf. Ser. 1963

(2021) 012058 https://doi.org/10.1088/1742-6596/1963/1/012058
[32] A. Keziz, M. Heraiz, F. Sahnoune, M. Rasheed, Ceram. Int. 49 (2023) 32989 https://doi.org/10.1016/j.ceramint.2023.07.275
[33] E. Kadri, K. Dhahri, R. Barillé, M. Rasheed. Phase Transitions 94 (2021) 65 https://doi.org/10.1080/01411594.2020.1832224
[34] D. Bouras, M. Rasheed, Opt. Quantum Electron. 54 (2022) 12 https://doi.org/10.1007/s11082-022-04161-1
[35] A. Zubaidi, L.M. Asaad, I. Alshalal, M. Rasheed, J. Mech. Behav. Mater. 32 (2023) 1 https://doi.org/10.1515/jmbm-2022-0302
[36] M. Rasheed et al., J. Phys.: Conf. Ser. 1999 (2021) 012080 https://doi.org/10.1088/1742-6596/1999/1/012080
[37] M. Rasheed, M.N. Al-Darraji, S. Shihab, A. Rashid, T. Rashid, J. Phys.: Conf. Ser. 1963 (2021) 012059 https://doi.org/10.1088/1742-6596/1963/1/012059
[38] M. Enneffatia, M. Rasheed, B. Louati, K. Guidara, S. Shihab, R. Barillé, J. Phys.: Conf. Ser. 1795 (2021) 012050. https://doi.org/10.1088/1742-6596/1795/1/012050
[39] M. Rasheed, O.Y. Mohammed, S. Shihab, A. Al-Adili, J. Phys.: Conf. Ser. 1795 (2021) 012043 https://doi.org/10.1088/1742-6596/1795/1/012043
[40] A.H. Ali, A.S. Jaber, M.T. Yaseen, M. Rasheed, O. Bazighifan, T.A. Nofal, Complexity 2022 (2022) 1 https://doi.org/10.1155/2022/9367638
[41] M. Rasheed, et al. J. Adv. Biotechnol. Exp. Ther. 6 (2023) 495 https://doi.org/10.5455/jabet.2023.d144
[42] M. Rasheed, I. Alshalal, A.A. Ashed, M.A. Sarhan, A.S. Jaber, Indones. J. Electr. Eng. Comput. Sci. 33 (2024) 653 https://doi.org/10.11591/ijeecs.v33.i1.pp653-660
[43] I.M. Mohammed, M. Rasheed, AIP Conf. Proc. 3321 (2025) 020026 https://doi.org/10.1063/5.0289719
[44] F. Boudou, A. Belakredar, A. Berkane, M. Rasheed, Not. Sci. Biol. 17 (2025) 12183 https://doi.org/10.55779/nsb17212183
[45] F. Boudou, et al., Not. Sci. Biol. 17 (2025) 12593 https://doi.org/10.55779/nsb17312593
[46] F. Boudou, A. Guendouzi, A. Belkredar, M. Rasheed, Not. Sci. Biol. 16 (2024) 13837 https://doi.org/10.55779/nsb16211837
[47] R.S. Mahmood, et al., J. Mech. Behav. Mater. 34 (2025) 1 https://doi.org/10.1515/jmbm-2025-0040
[48] T. Rashid, M.M. Mokji, M. Rasheed, J. Mech. Behav. Mater. 34 (2025) 77 https://doi.org/10.1515/jmbm-2025-0074
[49] M. Rasheed, M. N. Mohammedali, F. A. Sadiq, M. A. Sarhan, T. Saidani. J. Optics (New Delhi. Print) (2024) https://doi.org/10.1007/s12596-024-01928-5
[50] A.J. Hussein, M.N. Al-Darraji, M. Rasheed, M.A. Sarhan, IOP Conf. Ser.: Earth Environ. Sci. 1262 (2023) 022007 https://doi.org/ 10.1088/1755-1315/1262/2/022007
[51] A.J. Hussein, M.N. Al-Darraji, M. Rasheed, M.A. Sarhan, IOP Conf. Ser.: Earth Environ. Sci. 1262 (2023) 022005 https://doi.org/10.1088/1755-1315/1262/2/022005
[52] T. Saidani, M. Rasheed, I. Alshalal, A.A. Rashed, M.A. Sarhan, R. Barillé, Res. Eng. Struct. Mater. 10 (2024) 743 http://dx.doi.org/10.17515/resm2023.21ma0922rs
[53] A. M. Shehap, Kh.H. Mahmoud, M.F.H. Abdelkader, Tarek M. El-Basheer, Experimental and Theoretical NANOTECHNOLOGY 1 (2017) 103 https://doi.org/10.56053/1.2.103
[54] Badis Bendjemil, Mahiedinne Ali-Rachedi, Jamal Bougdira, Faming Zhang, Eberhard Burkel, Experimental and Theoretical NANOTECHNOLOGY 1 (2017) 145 https://doi.org/10.56053/1.3.145
[55] L.A. Carrero Bermúdez, R. Moreno Mendoza, R. Cardona, D.A. Landínez Téllez, J. Roa-Rojas, Experimental and Theoretical NANOTECHNOLOGY 1 (2017) 161 https://doi.org/10.56053/1.3.161

Exp. Theo. NANOTECHNOLOGY 10 (2026) 239-256